Supporting Information

Vellekoop et al. 10.1073/pnas.1319253111

SI Materials and Methods

Geological Setting. The K–Pg boundary deposits outcropping along the Brazos River between Waco and Hearne, Texas, comprise an exceptionally well-preserved sedimentary succession (1–9). In most previous studies, the K–Pg boundary interval has been subdivided in a series of lithological units (Units A to J) first described in ref. 3. The uppermost Maastrichtian Corsicana Formation consists of dark gray–brown mudstones, which are slightly laminated and include occasional shell hashes and other small mollusks. The top of the Corsicana Formation shows evidence of physical disruption with shell stringers and faint, plastically deformed clay clasts (Unit A). This soft-sediment deformation is most likely related to the force of the tsunami waves traversing the shelf. The basal coarse-grained part of the Paleocene Littig Member Unit B is scoured into Unit A and contains boulders and rip-up clasts. The Lower Littig Member consists of a distinct sequence of graded shell hashes, cross-bedded sands, and silts that is sometimes referred to as the K–Pg boundary "sandstone complex" (Units B–G) (7). The sandstone complex is further subdivided into a lower (B–D) and an upper complex (E–G). The lower complex is interpreted as tsunami deposits triggered by the Chicxulub impact on the Yucatan peninsula on present-day Mexico (3, 4, 6, 7, 10). Abundant altered impact spherules have been found in the lower B/C units (7), mixed in with backwashed local seafloor debris such as shell hash, fish teeth, glauconite pellets, and shallow-water foraminifera. Unit D consists of cross-bedded medium- to fine-grained sands, displaying mainly climbing-ripple tracts from the tsunami backwash. The sequence C–E may repeat locally up to four times, reflecting backwash from several individual tsunami surges. The upper complex of the K–Pg boundary sandstone complex comprises Units E, F, and G, grading from very fine sand to silt to mudstone. The base of this complex consists of a 1–2 cm thick siltstone (Unit E), overlain by a silty limestone (Unit F, 8 cm thick) and a subsequent gray claystone (Unit G, 10 cm). This complex shows a normal gradation and has previously been interpreted to be deposited within a time span of 24 h to weeks, as part of the settling phase of the tsunami/seiche complex deposited directly after the K–Pg boundary bolide impact (7) in the gulf. However, the iridium records already show elevated levels at the base of Unit E (1, 3, 11, 12) (Fig. S1). Because it may take days to years to deposit the very fine-grained impact-derived platinum group elements (PGEs) on the sea floor (13, 14), the complex of Units E–G probably represents a rapid depositional event that may have occurred at least weeks after the K–Pg boundary tsunami, largely as the deposition of suspended material after the waning of the tsunami waves, combined with disturbances by the large storms and hurricanes that occurred in the decades following the K–Pg boundary impact (15, 16) (see discussion under *SI Age Model*). The PGE-bearing, immediate postimpact sediments deposited directly on top of the tsunami deposit have probably been rapidly redeposited in the upper complex of Units E–G by these storms. This upper complex is overlain by a 5-cm-thick, laminated sandy bed with small shells and thin clay flakes (Unit H), which may represent a storm lag deposit of the last great storm passing this site. Following this is Unit I, a ∼2.5-m-thick silty claystone that is herein interpreted as representing the resumption of normal marine shelf sedimentation at this site. This unit is unconformably overlain by a conglomerate of the Kincaid Formation, the upper Littig Member (Unit J). This member is composed of a 0.3–0.6 m thick glauconitic sandy clay with grains, granules, and pebbles, followed by a marly claystone bed which forms the top of the section.

Sampling. At Brazos River, the Paleocene stratigraphy differs considerably from outcrop to outcrop (3), so first and last appearances and amount of reworking are difficult to compare between the various outcrops. The Brazos-1 outcrop (BR1), the first well-studied outcrop, has been partially destroyed due to sampling excavations and is currently inaccessible because of recent fluvial activity, which renders additional sampling difficult. Our analyses on organic-walled dinoflagellate cysts, biomarkers (TEX_{86}), planktic foraminifers, and grain size were all performed on a sample set acquired in 1995, when the outcrop was still relatively well exposed and accessible. This sample set was taken within a few meters from the section where Hansen et al. (3) and Jiang and Gartner (2) obtained their samples of mollusks and calcareous nannofossils (Fig. S2), minimizing the stratigraphic differences between our and the earlier published biostratigraphic results.

In the extensive 1995 sampling performed at BR1, great care was taken to acquire unweathered rock samples, to limit possible contamination by, for example, modern soil microbiota. A closely spaced sample set was obtained, to attain a high temporal resolution. The stratigraphic position was measured from the base of the graded silty limestone, Unit F, because this level is sharp, well visible, and constant throughout Brazos-1 and the other outcrops in the Brazos area. In total, about 100 samples were collected between 500 cm below the base of Unit F and 420 cm above the base of Unit F. The beds directly above the top of the sandstone (interval E–H) were sampled in large continuous blocks, which were slabbed in slices of 0.5-cm thickness. Unit I was sampled at 5-cm spacing in the first 2.5 m above the sandstone beds, the remainder to the Littig bed at 10 cm, and the top of the section at 25-cm intervals. The samples were split in aliquots for analysis of planktic and benthic foraminifers, organic-walled dinoflagellate cysts, and TEX_{86} analysis. All samples were oven-dried at 60 °C and stored at the VU University Amsterdam Faculty of Earth and Life Sciences sample storage. A selection of these samples was used in the present study.

Planktic Foraminifera. To construct a biostratigraphic framework for the section, 65 samples were weighed and washed over a nylon mesh of 63 μm. A split of the >63μ fraction was analyzed using a binocular at magnification of 125×, and from the >124μ fraction, about 200–400 specimens were randomly picked and counted. The remaining residue was searched for rare specimens and species.

Palynology. Palynological processing followed the standardized quantitative methods used at the Laboratory of Paleobotany and Palynology, Utrecht University (17). Briefly, ∼10 g of each sample was crushed, oven dried (60 °C), and weighed, and a known amount (10,679, $1\sigma = 5\%$) of modern *Lycopodium clavatum* spores was added. The samples were then treated with 10% HCl and subsequently with 40% HF to dissolve carbonate and siliceous components, respectively. The residue was sieved over nylon mesh sieves of 250 μm and 15 μm. From the residue of the 15–250 μm fraction, quantitative slides were made on well-mixed representative fractions. In the present study, 84 samples were analyzed for palynology. Per sample, a minimum of 200 dinocysts was identified to the species level at ∼500× magnification.

Organic Geochemical Analyses. Organic compounds were extracted from powdered and freeze-dried rock samples of ~10 g with dichloromethane (DCM)/methanol (MeOH) [9:1 (vol/vol)] using a DIONEX accelerated solvent extractor (ASE 200) at a temperature of 100 °C and a pressure of 7.6 × 106 Pa. Excess solvent was removed by means of rotary evaporation under near-vacuum. The total extracts were separated in four fractions over an activated Al_2O_3 column successively using hexane:dichloromethane (DCM) [9:1 (vol/vol)], ethyl acetate (100%), DCM:MeOH [95:5 (vol/vol)], and DCM:MeOH [1:1 (vol/vol)].

Following this, 250 ng of a C_{46} Glycerol Trialkyl Glycerol Tetraether internal standard (18) was added to the DCM:MeOH [95:5 (vol/vol)] fraction for quantification purposes. This fraction was subsequently dried and redissolved in a hexane:isopropanol [99:1 (vol/vol)] solvent mixture and filtered using a 0.45-μm mesh, 4-mm-diameter polytetrafluoroethylene (PTFE) filter before analysis. Samples were analyzed using high-performance liquid chromatography/atmospheric pressure positive ion chemical ionization mass spectrometry (HPLC/APCI-MS).

HPLC/APCI-MS analyses were performed according to ref. 19, using an Agilent 1100 series LC/MSD SL (Liquid Chromatography/Mass Spectrometric Detector type SL) and separation over a Prevail Cyano column (2.1 × 150 mm, 3 μm; Alltech), maintained at 30 °C. Glycerol Dibiphytanyl Glycerol Tetraethers (GDGTs) were eluted using the following gradient in the hexane:isopropanol mixture as follows: hexane:propanol [99:1 (vol/vol)] for 5 min, then a linear gradient to hexane: propanol [98.2:1.8 (vol/vol)] in 45 min, with a flow rate of 0.2 $mL{\cdot}min^{-1}$. Selective ion monitoring was set to scan the 8 $[M+H]^+$ ions of the GDGTs. The TEX_{86} index values were calculated following ref. 20. Because we apply the TEX_{86} paleothermometer on samples from a midlatitude site from a Cretaceous–Paleogene greenhouse world, unambiguously characterized by high sea surface temperatures (SSTs) (>15 °C), we applied the TEX_{86}^H calibration from ref. 21 to translate TEX_{86} index values to mean annual sea surface temperature:

$$SST = 68.4 \times TEX_{86}^H + 38.6, \quad \textbf{[S1]}$$

where

$$TEX_{86}^H = \log(TEX_{86}), \quad \textbf{[S2]}$$

and

$$TEX_{86} = \frac{[GDGT-2] + [GDGT-3] + [Cren']}{[GDGT-1] + [GDGT-2] + [GDGT-3] + [Cren']}, \quad \textbf{[S3]}$$

where GDGT numbers refer to fig. 1 in Kim et al. (21).

Grain Size Analysis. The grain size distribution of each sample was determined in the same manner as the 1994 sample set described in ref. 7. The grain size distributions were determined on a Fritsch A-22 laser particle sizer. Each sample was first dissolved in HCL to remove all calcareous fossil and authigenic carbonate material, and the insoluble residue was subsequently treated with 20% H_2O_2 to remove, e.g., authigenic phases like pyrite and organic material. The remaining residue was dissolved in water with added $Na_2(P_2O_5)$ to prevent coagulation of clay particles during the analytical runs. The laser diffraction patterns were translated into a grain size distribution according to the Fraunhofer model. In Fig. S3 the mean grain size is drawn, showing the siliciclastic grain size of the tsunamigenic cross-bedded sands of units B–E, followed by the overall graded units F–I.

SI Age Model

Iridium. The high-resolution age model used in this study is based on the Ir anomaly and calcareous nannoplankton, planktic foraminifer, and organic-walled dinoflagellate cyst (dinocyst) biostratigraphy (Fig. S3). Various studies have been published on the iridium anomalies at the sites in the Brazos River area (1, 11, 12, 22), showing a series of irregular peaks in lithological Units E, F, and G. (Fig. S1). It is likely that the PGE-bearing impact dust settled within months to years after the impact and was subsequently reworked in the lag deposits of postimpact storms (13, 14), explaining the scattered and smeared out nature of the iridium profile. Because the enhanced contrast between warm oceans and cold atmosphere, triggering the storms after the impact, likely lasted for less than a century (23), we assume that this is the maximum amount of time represented by Units E, F, and G.

Nannofossils. Jiang and Gartner (2) published detailed, semiquantitative nannofossil data from a closely spaced sample set from the same Brazos-1 locality. Based on the lateral lithological continuity at this site we assume that their results can be tied in with our biostratigraphic data (Fig. S3), although they did not specifically mention the limestone of Unit F. They demonstrated that the top of the Corsicana Formation comprises the uppermost Maastrichtian *Micula murus* Zone and that the overlying Kincaid Formation contains a rapid succession of basal Paleocene assemblages, thereby recognizing that the contact between these two formations represents the K–Pg boundary. The basal meter of the Kincaid Fm, above the tsunami K–Pg boundary sandstone complex, is dominated by inferred disaster taxa, such as species of the calcareous dinoflagellate cyst genus *Thoracosphaera* and the calcareous nannoplankton species *Braarudosphaera bigelowii*. Blooms of *Thoracosphaera* have been recorded in the earliest Paleocene at many different sites (24, 25) and are considered a characteristic feature for the lowermost Danian. The first true Paleocene nannoplankton species (*Biscutum romeinii*) occurs ~1 m above the base of the Kincaid Formation (see fig. 3 of ref. 2).

Planktic Foraminifera. The foraminiferal biozonation applied in this paper largely follows ref. 26, with a few refinements of the basalmost Paleocene as already discussed in ref. 27 (Figs. S3–S5). The biostratigraphically important datum events of the earliest Paleocene species are discussed here (*Taxonomic Notes on Planktic Foraminifera*).

The Maastrichtian samples Br95-61/70 (see Table S1 for a sample list) contain well-preserved, moderately abundant Maastrichtian planktic foraminiferal assemblages. However, the larger species such as *Globotruncana contusa*, *Globotruncana stuarti*, *Racemiguembelina fructicosa* and *Abathomphalus mayaroensis* are missing due to the shallow paleodepth of the Brazos sections. The planktic/benthic foraminifer ratio is around 30–50%, indicating outer shelf conditions, indicative of a water depth of 50–100 m.

The first Paleocene taxon, *Parvulorugoglobigerina minutula* (*Globigerina extensa* in the sense of ref. 26), appears in Br95-23, followed by the first appearance datum (FAD) of *Parvulorugoglobigerina alabamensis* (*Globigerina fringa* in the sense of ref. 27) in sample Br95-24. *Chiloguembelina* sp. and *Woodringina* sp. appear in sample Br95-30. These taxa are initially very rare and do not show up in the counts of 300 random selected specimens. *P. eugubina* appears in sample Br95-26. This sequence of FADs, *P. minutula–P. alabamensis–Parvulorugoglobigerina eugubina*, is remarkably similar to the expanded lowermost Paleocene section of el Kef in Tunisia (26) and demonstrates that the zonation presented in Fig. S5 is valid for extremely expanded sections for lower northern subtropical latitudes. In the majority of expanded and complete sections (such as Zumaya, Agost, and Caravaca in

Spain; the Apennine sections in Italy; and Bjala in Bulgaria) such successive first appearances cannot be distinguished, probably because of the homogenization by bioturbation. Biozone P0—or *Guembelitria cretacea* zone—therefore attains a thickness in Brazos-1 of around 90 cm, all in background outer shelf mudstones (Unit I), disregarding the combined thickness of 50 cm of the size-graded tsunami and storm-induced coarse-grained layers (Units A–H).

Organic-Walled Dinoflagellate Cysts. Various studies have shown that organic-walled cyst-producing dinoflagellates do not experience extinctions across the K–Pg boundary. In contrast, they display a rapid succession of qualitative and quantitative events within planktic foraminiferal zone P0 that provides the basis for a high-resolution biostratigraphy for the lowermost Danian (28, 29). The most important biostratigraphical dinocyst dates for the earliest Danian are the first occurrences of, subsequently, *Senoniasphaera inornata*, *Damassadinium californicum*, and *Carpatella cornuta* (28, 29). Also typical for dinocyst development across the K–Pg boundary are morphological changes of representatives of the fibrous cribroperidinioids (cf. ref. 30), such as *Cordosphaeridium* spp., *Disphaerogena* spp. and *Cribroperidinium* spp. These changes involve the formation of distinct antapical and apical horns and in some genera strong variance of process types. The first signs of these morphological changes are found in *Disphaerogena carposphaeropsis*, which forms an antapical and an apical horn and first occurs in the uppermost Maastrichtian in K–Pg boundary sections around the world (28, 31).

Based on the lowermost and uppermost occurrences of stratigraphically important dinocyst species and forms, a dinocyst zonation can be produced for BR1 (Fig. S5). The uppermost Maastrichtian biostratigraphic marker *D. carposphaeropsis* with the typical apical and antapical horn (i.e., *D. carposphaeropsis* var. cornuta) is found throughout the studied interval. The first lowermost Danian biostratigraphic marker *S. cf inornata* is found just beneath lithological Unit H, ∼20 cm above the base of Unit F, in sample Br95-4b. This further substantiates that little time is represented by lithological Units E, F, and G. The stratigraphically important species *S. cf inornata* differs slightly from *S. inornata* (for taxonomic notes on the dinocysts encountered in BR1, see *SI Taxonomic Notes on Organic-Walled Dinoflagellate Cysts*), which is found higher up in the section at the base of the Littig Member. The marker species *D. cf californicum* first appears in Br95-14, 65 cm above the base of Unit F, and the global biostratigraphic markers *D. californicum* and *C. cornuta* have their FAD at the base of the upper Littig members of the Kincaid Formation.

SI Application of TEX_{86}

Introduction. The TEX_{86} SST proxy is based on the relative distribution of cyclopentane-containing isoprenoid GDGT lipids in the membranes of marine Thaumarchaeota (20, 21). These organisms have been shown to adjust the composition of these membrane lipids in response to changes in growth temperature (32). The distribution pattern is quantified as the so-called TEX_{86} (Tetraether index of 86 carbon atoms). This index shows a strong correlation with SST and appears to be independent of the initial seawater chemistry (20, 21, 32, 33). Therefore, TEX_{86} provides a means of reconstructing past mean annual average SSTs based on the tetraether membrane lipid composition preserved in sediments and sedimentary rocks (20).

The TEX_{86} paleothermometer has been successfully applied on a variety of Neogene, Paleogene, and Cretaceous sites by various laboratories (34–39). Although the absolute values of the reconstructed temperatures are still subject of discussion, particularly at temperatures beyond the modern core top calibration, the trends in TEX_{86} records are generally in good agreement with other paleothermometers ($\delta^{18}O$, Mg/Ca, and $U^{K'}_{37}$) and reflect known climate events, e.g., warming during the Paleocene Eocene climatic optimum and late Eocene cooling (34–36, 40–42).

Potential Biases on TEX_{86}. High concentrations of soil organic matter (SOM) in sediments can cause a substantial bias in TEX_{86}-reconstructed sea surface temperatures (43). In outcrop sections, possible contamination with GDGTs derived from modern soil bacteria often further hampers the application of the TEX_{86} paleothermometer. The relative amount of SOM in sediments can be approximated based on the analysis of tetraether lipids, using the so-called Branched and Isoprenoid Tetraether (BIT) index (44). To identify whether our TEX_{86} record is biased by the input of SOM, we have calculated the BIT index for all our samples. In our record, there is no significant correlation between TEX_{86} and the BIT-index ($R^2 = 0.0008$, P value = 0.822; Fig. S6), indicating that SOM in our samples did not bias our TEX_{86} record significantly. To nevertheless exclude all TEX_{86}-reconstructed sea surface temperatures possibly biased by high concentrations of terrestrial-derived GDGTs, we discarded samples with a BIT-index exceeding the recommended (43) threshold of 0.3 (Fig. S6). A striking aspect of our BIT index record is the occurrence of prominent peaks of ∼0.5 and ∼0.65 in the tsunami deposit and lithological Unit H, respectively, superimposed on background values of ∼0.1–0.2 (Fig. S7). It is expected that backwash deposits of a tsunami comprise higher concentrations of terrestrial derived organic matter, potentially explaining this peak in the BIT record. Conversely, the larger grain size and higher porosity of these beds (7) make them more prone to meteoric diagenesis and contamination with modern soil-derived organic material by percolating water. Hence, the peaks in the BIT record might also reflect input of modern soil-derived organic material.

Another possible bias in TEX_{86} paleothermometry can be introduced by the input of methanogenic and methanotrophic archaeal GDGTs, leading to erroneous SST reconstructions (45–47). Potential contribution of methanogenic and methanotrophic archaeal GDGTs can be recognized using the ratio of GDGT-0/Crenarchaeol (45) and the Methane Index (47), respectively. In our study, the GDGT-0/Crenarchaeol ratio ranges between 0.08 and 1.01, well below the recommended threshold of 2.0 (45), whereas the Methane Index ranges between 0.10 and 0.30, below the recommended threshold of 0.5 (47). These values suggest that at BR1, there is little input of GDGTs derived from methanogenic or methanotrophic archaea.

Accuracy of TEX_{86} Temperature Estimates. In the samples analyzed for this study, concentrations of isoprenoidal GDGTs range from 0.2 to 2 ng/g dry weight sediment. The overall chromatography of the GDGTs was good, with proper signal to noise ratios (Fig. S8). To test the reproducibility of these signals, ∼10% of the samples were extracted and analyzed in duplicate. Of the samples, all but one had reproducibility better than 0.25 °C (Fig. S9). In one occasion (sample Br95-1G) a duplicate analysis resulted in a temperature difference of 1.1 °C. However, we cannot exclude that this difference actually reflects original sediment heterogeneity. This particular sample originates from lithological Unit F, interpreted as a mixed storm lag deposit. Therefore, it is likely that this rock sample consists of a nonhomogeneous mixture of uppermost Maastrichtian material and immediate postimpact materials. Similar discrepancies have been documented in the iridium analyses of this interval (*Iridium*).

The calibration used in this study has a SE of ±2.5 °C (22). The reconstructed absolute temperatures should be interpreted with care, but here we are more concerned with trends, i.e., changes in ocean temperature rather than absolute temperatures. Although TEX_{86} is calibrated to SST (20), various studies suggested that TEX_{86} might sometimes reflect deeper water temperatures (48, 49). However, the studied section was deposited at a shallow, shelf

depositional environment (4, 7), excluding the possibility that the recorded trends would significantly differ from trends in SSTs.

Other potential problems with our TEX_{86} record include possible changes in ecology of Thaumarchaeota, e.g., a switch in growing season from summer to winter. However, in the K–Pg boundary greenhouse, subtropical sites such as BR1 likely experienced a much smaller seasonality (50, 51). Therefore, possible temperature effects of changes in growing season will be limited at BR1. Instead, our data demonstrate that the postimpact world was characterized by cool conditions for decades.

SI Taxonomic Notes on Planktic Foraminifera

***P. minutula* (Luterbacher and Premoli Silva).** Smit (27) described specimens from El Kef, Tunisia, that are the oldest Paleocene planktic foraminifers as *Globigerina minutula*. This taxon has the typical smooth, microperforate wall textures as *P. alabamensis* and *P. eugubina* and is probably a derived taxon from *G. cretacea* (26). However, we do not follow Olsson et al. (26) in placing this taxon in *P. extensa* (Blow) because we regard, after study of the material of the type locality of *P. minutula* in Ceselli in the Apennines, *P. extensa* (in the sense of ref. 26) as a junior synonym of *P. minutula.* Likewise, *Globoconusa conusa* (in the sense of ref. 52) is a synonym of *P. minutula*.

***P. alabamensis* (Olsson 1999).** Smit (27, 53) described specimens of this taxon from Caravaca and el Kef as *G. fringa*. However, Olsson et al. (26) demonstrated that the original holotype specimens of *P. fringa* (subbotina) are from a small cancellate species, more similar to *Eoglobigerina* spp. but unlike the specimens considered earlier as *P. fringa*. These specimens are closely similar to *P. alabamensis* (26), and we place them in that taxon.

Taxonomic Notes on Organic-Walled Dinoflagellate Cysts

***Carpatella* cf cornuta.** This morphotype differs from *Carpatella cornuta* by having a less thick wall. In this study it is regarded as a transitional form between *Cribroperidinium sp. A* of Brinkhuis and Schioler, 1996, and *C. cornuta* s.s.

***Cordosphaeridium fibrospinosum* var. *cornuta*.** This taxon differs from *C. fibrospinosum* by the development of distinct apical and antapical horns.

***Damassadinium cf californicum*.** This morphotype is distinguished from *Damassadinium californicum* by having a less broad process base. In this study, this morphotype is regarded as a predecessor for *D. californicum* s.s.

***Disphaerogena carposphaeropsis* var. *cornuta*.** This morphotype is distinguished from *Disphaerogena carposphaeropsis* by having formed an apical horn and larger antapical horn. This morphotype is very characteristic for the uppermost Maastrichtian and earliest Danian.

***Senoniasphaera* cf inornata.** This morphotype differs from *Senoniasphaera inornata* by having a smaller size and thinner outer wall. In this study this morphotype is regarded as a predecessor for *S. inornata* s.s.

1. Ganapathy R, Gartner S (1981) Ming-Jung Jiang, Iridium anomaly at the Cretaceous-Tertiary boundary in Texas. *Earth Planet Sci Lett* 54(3):393–396.
2. Jiang MJ, Gartner S (1986) Calcareous nannofossil succession across the Cretaceous/Tertiary boundary in east-central Texas. *Micropaleontology* 32(3):232–255.
3. Hansen TA, Farrand RB, Montgomery HA, Billman HG, Blechschmidt GL (1987) Sedimentology and extinction patterns across the Cretaceous-Tertiary boundary interval in East Texas. *Cretac Res* 8(3):229–252.
4. Bourgeois J, Hansen TA, Wiberg PL, Kauffman EG (1988) A tsunami deposit at the cretaceous-tertiary boundary in Texas. *Science* 241(4865):567–570.
5. Keller G (1989) Extended Cretaceous/Tertiary boundary extinctions and delayed population change in planktonic foraminifers from Brazos River, Texas. *Paleoceanography* 4(3):287–332.
6. Yancey TE (1996) Stratigraphy and depositional environments of the Cretaceous/Tertiary boundary complex and basal section, Brazos River, Texas. *Gulf Coast Assoc Geol Soc Trans* 46:433–442.
7. Smit J, et al. (1996) Coarse-grained, clastic sandstone complex at the K/T boundary around the Gulf of Mexico: Deposition by tsunami waves induced by the Chicxulub impact? *Spec Pap Geol Soc Am* 307:151–182.
8. Heymann D, et al. (1998) Geochemical markers of the Cretaceous–Tertiary boundary event at Brazos River, Texas, USA. *Geochim Cosmochim Acta* 62(1):173–181.
9. Schulte P, Speijer R, Mai H, Kontny A (2006) The Cretaceous–Paleogene (K–P) boundary at Brazos, Texas: Sequence stratigraphy, depositional events and the Chicxulub impact. *Sediment Geol* 184(1-2):77–109.
10. Hildebrand AR, et al. (1991) Chicxulub crater: A possible Cretaceous/Tertiary boundary impact crater on the Yucatán peninsula, Mexico. *Geology* 19(9):867–871.
11. Asaro F, Michel HV, Alvarez LW, Maddocks RF, Bunch T (1982) Iridium and other geochemical profiles near the Cretaceous-Tertiary boundary in a Brazos river section in Texas. *Texas ostracoda, International Symposium on Ostracoda, 8th, Guidebook of Excursion and Related Papers*, ed Maddocks RF (Univ of Houston, Houston), pp 238–241.
12. Rocchia R, Robin E, Froget L, Gayraud J (1996) Stratigraphic distribution of extraterrestrial markers at the Cretaceous-Tertiary boundary in the Gulf of Mexico area: Implications for the temporal complexity of the event. *Spec Pap Geol Soc Am* 307:279–286.
13. Robin E, et al. (1991) The stratigraphic distribution of Ni-rich spinels in Cretaceous-Tertiary boundary rocks at E1 Kef (Tunisia), Caravaca (Spain) and Hole 761C (Leg 122). *Earth Planet Sci Lett* 107(3-4):715–721.
14. Kring DA, Durda DD (2002) Trajectories and distribution of material ejected from the Chicxulub impact crater: Implications for postimpact wildfires. *J Geophys Res* 107(8):5062.
15. Emanuel KA, Speer K, Rotunno R, Srivastava R, Molina M (1995) Hypercanes: A possible link in global extinction scenarios. *J Geophys Res* 100(D7):13755–13765.
16. Hart MB, et al. (2012) The Cretaceous-Paleogene boundary on the Brazos River, Texas: New stratigraphic sections and revised interpretations. *GCAGS J* 1:69–80.
17. Houben AJP, Bijl PK, Guerstein GR, Sluijs A, Brinkhuis H (2011) Malvinia escutiana, a new biostratigraphically important Oligocene dinoflagellate cyst from the Southern Ocean. *Rev Palaeobot Palynol* 165(3-4):175–182.
18. Huguet C, et al. (2006) An improved method to determine the absolute abundance of glycerol dibiphytanyl glycerol tetraether lipids. *Org Geochem* 37(9): 1036–1041.
19. Schouten S, Huguet C, Hopmans EC, Kienhuis MV, Damsté JS (2007) Analytical methodology for TEX86 paleothermometry by high-performance liquid chromatography/atmospheric pressure chemical ionization-mass spectrometry. *Anal Chem* 79(7): 2940–2944.
20. Schouten S, Hopmans EC, Schefuss E, Sinninghe Damsté JS (2002) Distributional variations in marine crenarchaeotal membrane lipids: A new organic proxy for reconstructing ancient sea water temperatures? *Earth Planet Sci Lett* 204(1):265–274.
21. Kim JH, et al. (2010) New indices and calibrations derived from the distribution of crenarchaeal isoprenoid tetraether lipids: Implications for past sea surface temperature reconstructions. *Geochim Cosmochim Acta* 74(16):4639–4654.
22. Hansen TA, Upshaw B III, Kauffman EG, Gose W (1993) Patterns of molluscan extinction and recovery across the Cretaceous–Tertiary boundary in east Texas: Report on new outcrops. *Cretac Res* 14(6):685–706.
23. Galeotti S, Brinkhuis H, Huber M (2004) Records of post–Cretaceous-Tertiary boundary millennial-scale cooling from the western Tethys: A smoking gun for the impact-winter hypothesis? *Geology* 32(6):529–532.
24. Gardin S (2002) Late Maastrichtian to early Danian calcareous nannofossils at Elles (northwest Tunisia): A tale of one million years across the K/T boundary. *Palaeogeogr Palaeoclimatol Palaeoecol* 178(3-4):211–231.
25. Lottaroli F, Catrullo D (2000) The calcareous nannofossil biostratigraphic framework of the Late Maastrichtian–Danian North Sea chalk. *Mar Micropaleontol* 39(1-4):239–263.
26. Olsson RK, et al. (1999) *Atlas of Paleogene Planktonic Foraminifera* (Smithsonian Contributions to Paleobiology, Washington, DC), p 225.
27. Smit J (1982) Extinction and evolution of planktonic foraminifera after a major impact at the Cretaceous/Tertiary boundary. *Spec Pap Geol Soc Am* 190:329–352.
28. Moshkovitz S, Habib D (1993) Calcareous nannofossil and dinoflagellate stratigraphy of the Cretaceous-Tertiary boundary, Alabama and Georgia. *Micropaleontology* 39(2):167–191.
29. Brinkhuis H, Bujak JP, Smit J, Versteegh GJM, Visscher H (1998) Dinoflagellate-based sea surface temperature reconstructions across the Cretaceous–Tertiary boundary. *Palaeogeogr Palaeoclimatol Palaeoecol* 141(1-2):67–83.
30. Sluijs A, Brinkhuis H (2009) A dynamic climate and ecosystem state during the Paleocene-Eocene Thermal Maximum: Inferences from dinoflagellate cyst assemblages on the New Jersey Shelf. *Biogeosciences* 6(8):1755–1781.
31. Prámparo M, Papú OH (2006) Late Maastrichtian dinoflagellate cysts from the Cerro Butaló section, southern Mendoza province, Argentina. *J Micropaleontol* 25(1):23–33.
32. Wuchter C, Schouten S, Coolen MJL, Sinninghe Damsté JS (2004) Temperature-dependent variation in the distribution of tetraether membrane lipids of marine Crenarchaeota: Implications for TEX86 paleothermometry. *Paleoceanography* 19(4): PA4028.
33. Kim JH, Schouten S, Hopmans EC, Donner B, Sinninghe Damsté JS (2008) Global sediment core-top calibration of the TEX_{86} paleothermometer in the ocean. *Geochim Cosmochim Acta* 72(4):1154–1173.

34. Schouten S, et al. (2003) Extremely high sea-surface temperatures at low latitudes during the middle Cretaceous as revealed by archaeal membrane lipids. *Geology* 31(12):1069–1072.
35. Forster A, Schouten S, Baas M, Sinninghe Damsté JS (2007) Mid-Cretaceous (Albian-Santonian) sea surface temperature record of the tropical Atlantic Ocean. *Geology* 35(10):919–922.
36. Sluijs A, et al. (2007) Environmental precursors to rapid light carbon injection at the Palaeocene/Eocene boundary. *Nature* 450(7173):1218–1221.
37. Bijl PK, et al. (2010) Transient Middle Eocene atmospheric CO_2 and temperature variations. *Science* 330(6005):819–821.
38. Littler K, Robinson SA, Bown PR, Nederbragt AJ, Pancost RD (2011) High sea-surface temperatures during the Early Cretaceous Epoch. *Nat Geosci* 4(3):169–172.
39. Seki O, et al. (2012) Paleoceanographic changes in the Eastern Equatorial Pacific over the last 10 Myr. *Paleoceanography* 27(3):PA3224.
40. Hollis CJ, et al. (2009) Tropical sea temperatures in the high-latitude South Pacific during the Eocene. *Geology* 37(2):99–102.
41. Liu Z, et al. (2009) Global cooling during the Eocene-Oligocene climate transition. *Science* 323(5918):1187–1190.
42. Wade BS, et al. (2012) Multiproxy record of abrupt sea-surface cooling across the Eocene-Oligocene transition in the Gulf of Mexico. *Geology* 40(2):159–162.
43. Weijers JWH, Schouten S, Spaargaren OC, Sinninghe-Damsté JS (2006) Occurrence and distribution of tetraether membrane lipids in soils: Implications for the use of the TEX86 proxy and the BIT index. *Org Geochem* 37(12):1680–1693.
44. Hopmans EC, et al. (2004) A novel proxy for terrestrial organic matter in sediments based on branched and isoprenoid tetraether lipids. *Earth Planet Sci Lett* 224(1-2):107–116.
45. Blaga CI, Reichart GJ, Heiri O, Sinninghe Damsté JS (2009) Tetraether membrane lipid distributions in lake particulate matter and sediments: A study of 47 European lakes along a North-South transect. *J Paleolimnol* 41(3):523–540.
46. Weijers JWH, Lim KLH, Aquilina A, Sinninghe Damsté JS, Pancost RD (2011) Biogeochemical controls on glycerol dialkyl glycerol tetraether lipid distributions in sediments characterized by diffusive methane flux. *Geochem Geophys Geosyst* 12(10): Q10010.
47. Zhang YG, et al. (2011) Methane index: A tetraether archaeal lipid biomarker indicator for detecting the instability of marine gas hydrates. *Earth Planet Sci Lett* 307(3-4):525–534.
48. Huguet C, et al. (2007) A study of the TEX_{86} paleothermometer in the water column and sediments of the Santa Barbara Basin, California. *Paleoceanography* 22(3): PA3203.
49. Lopes dos Santos R, et al. (2010) Glacial-interglacial variability in Atlantic meridional overturning circulation and thermocline adjustments in the tropical North Atlantic. *Earth Planet Sci Lett* 300(3-4):407–414.
50. Steuber T, Rauch M, Masse JP, Graaf J, Malkoc M (2005) Low-latitude seasonality of Cretaceous temperatures in warm and cold episodes. *Nature* 437(7063):1341–1344.
51. Donnadieu Y, Pierrehumbert R, Jacob R, Fluteau F (2006) Modelling the primary control of paleogeography on Cretaceous climate. *Earth Planet Sci Lett* 248(1-2): 426–437.
52. Keller G (1988) Extinction, survivorship and evolution of planktic foraminifera across the Cretaceous/Tertiary boundary at El Kef, Tunisia. *Mar Micropaleontol* 13(3): 239–263.
53. Smit J (1977) Discovery of a planktonic foraminiferal association between the Abathomphalus mayaroensis zone and the "Globigerina" eugubina zone at the Cretaceous/Tertiary boundary in the Barranco del Gredero (Caravaca, SE Spain): A preliminary report. *Proc K Ned Akad Wet* 80:280–301.

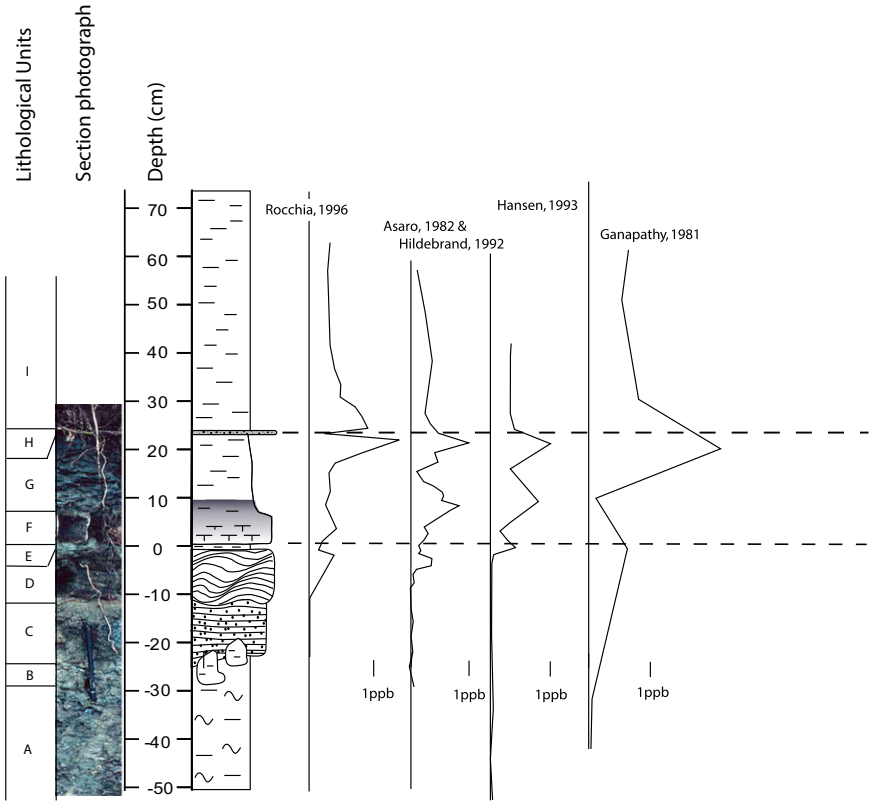

Fig. S1. Compilation of published iridium profiles from the Brazos-1 section. These profiles can be directly compared because they were sampled within a few m from each other.

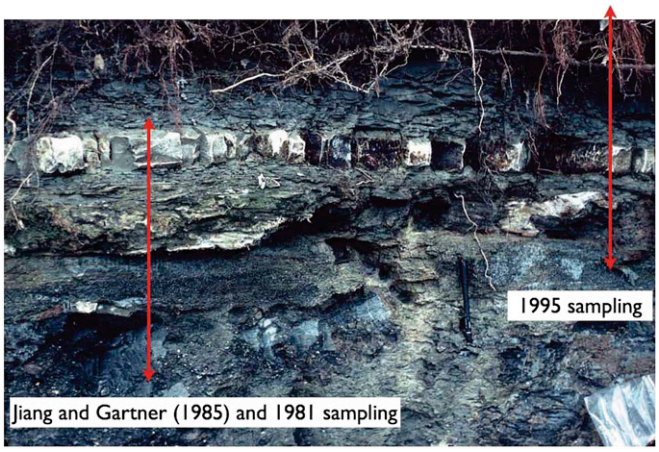

Fig. S2. Brazos-1 outcrop situation in 1981, when the outcrop was still easily accessible. See pen for scale.

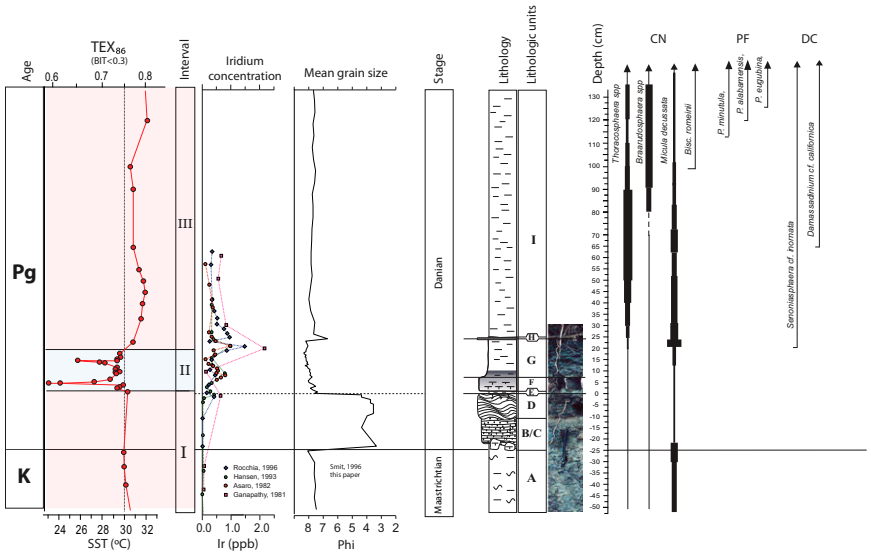

Fig. S3. Biomarker ranges of the K–Pg interval of the Brazos-1 section, compared with the TEX_{86} profile, iridium concentrations, grain size distribution on the Krumbein phi (φ) scale, and lithology. The calcareous nannofossil (CN) markers are from Jiang and Gartner (2). Planktic foraminiferal (PF) and dinocyst (DC) ranges are new data in this paper.

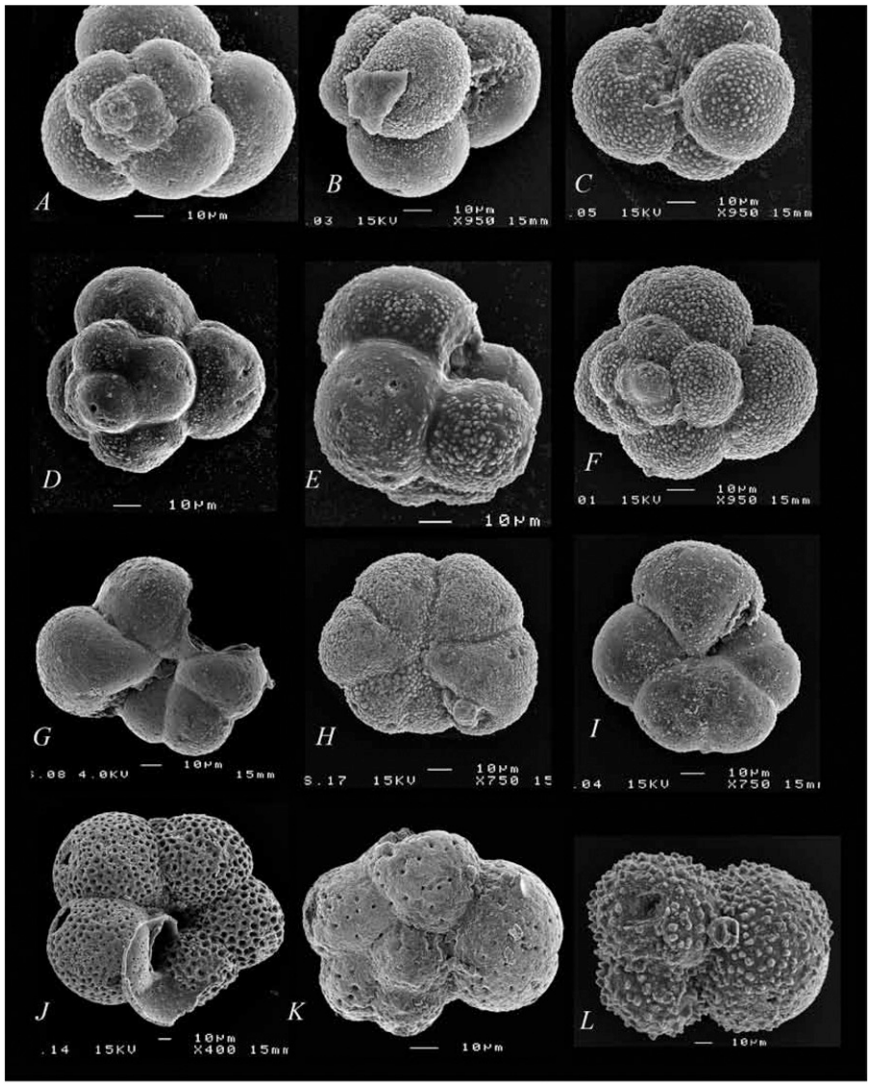

Fig. S4. Important planktic foraminiferal biomarkers from the Brazos-1 section. (*A*–*C*) *P. minutula*, Br95-29. (*D*–*F*) *P. alabamensis*: (*D* and *E*) Br95-29 and (*F*) Br95-29. (*G*–*I*) *P. eugubinai*: (*G*) Br95-27, (*H*) Br95-31, and (*I*) Br95-45. (*J*) *Morozovella pseudobulloides*, Br95-59. (*K*) *Eoglobigerina eobulloides*, Br95-47. (*L*) *Globoconusa daubjergensis*, Br95-46.

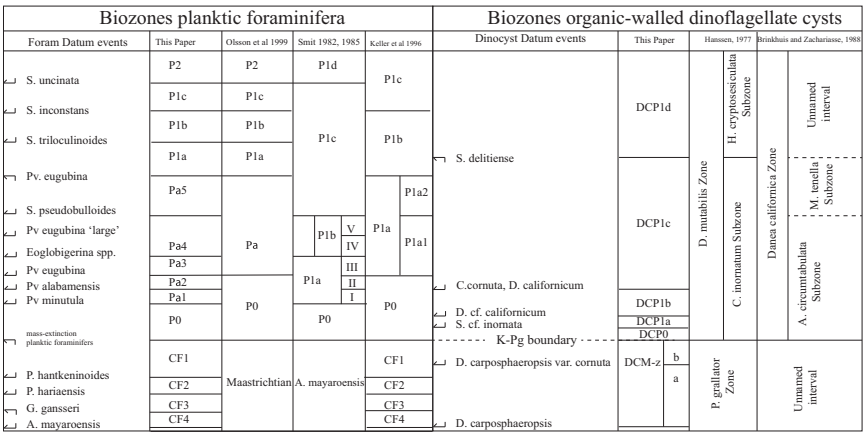

Fig. S5. Foraminiferal and organic-walled dinoflagellate cyst zonal scheme used in this paper. The interval of the basal-most Danian is subdivided on the FADs of earliest Danian species, allowing for a comparison with other expanded sections, such as at El Kef, Tunisia.

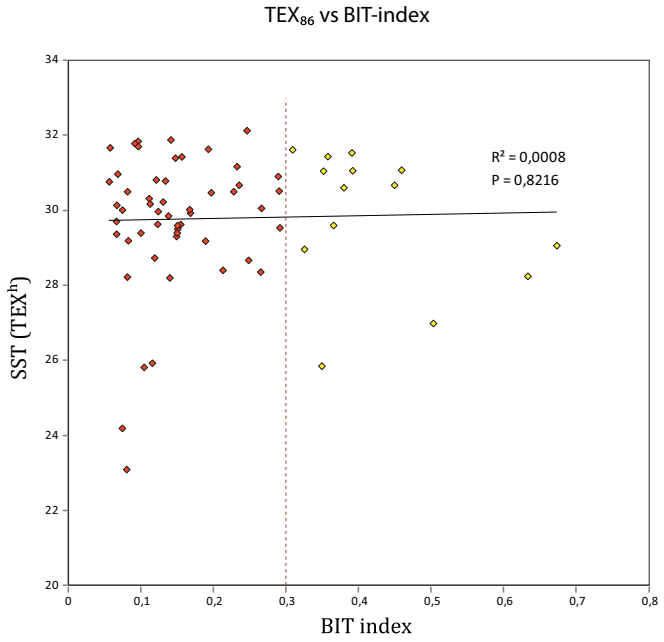

Fig. S6. TEX_{86}-derived sea surface temperatures plotted against BIT-index values. This plot indicates that there is no statistically significant correlation between SST and BIT, signifying that our TEX_{86} record is not significantly biased by soil organic matter in our samples. Nevertheless, all samples with a BIT-index exceeding the recommended threshold of 0.3 (red diamonds) are discarded following ref. 43.

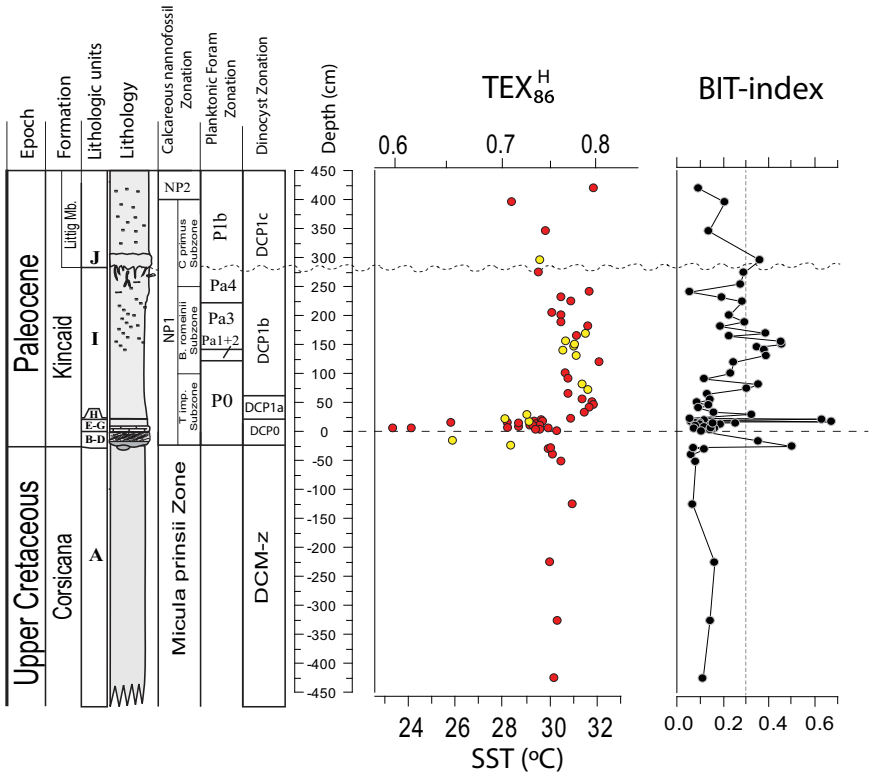

Fig. S7. TEX_{86} record and BIT-index record of Brazos River. The recommended threshold of 0.3 of ref. 43 is indicated in the BIT-index graph. In the TEX_{86} record, red dots indicate samples with a BIT-index below 0.3, and yellow dots indicate samples with a BIT-index value exceeding 0.3.

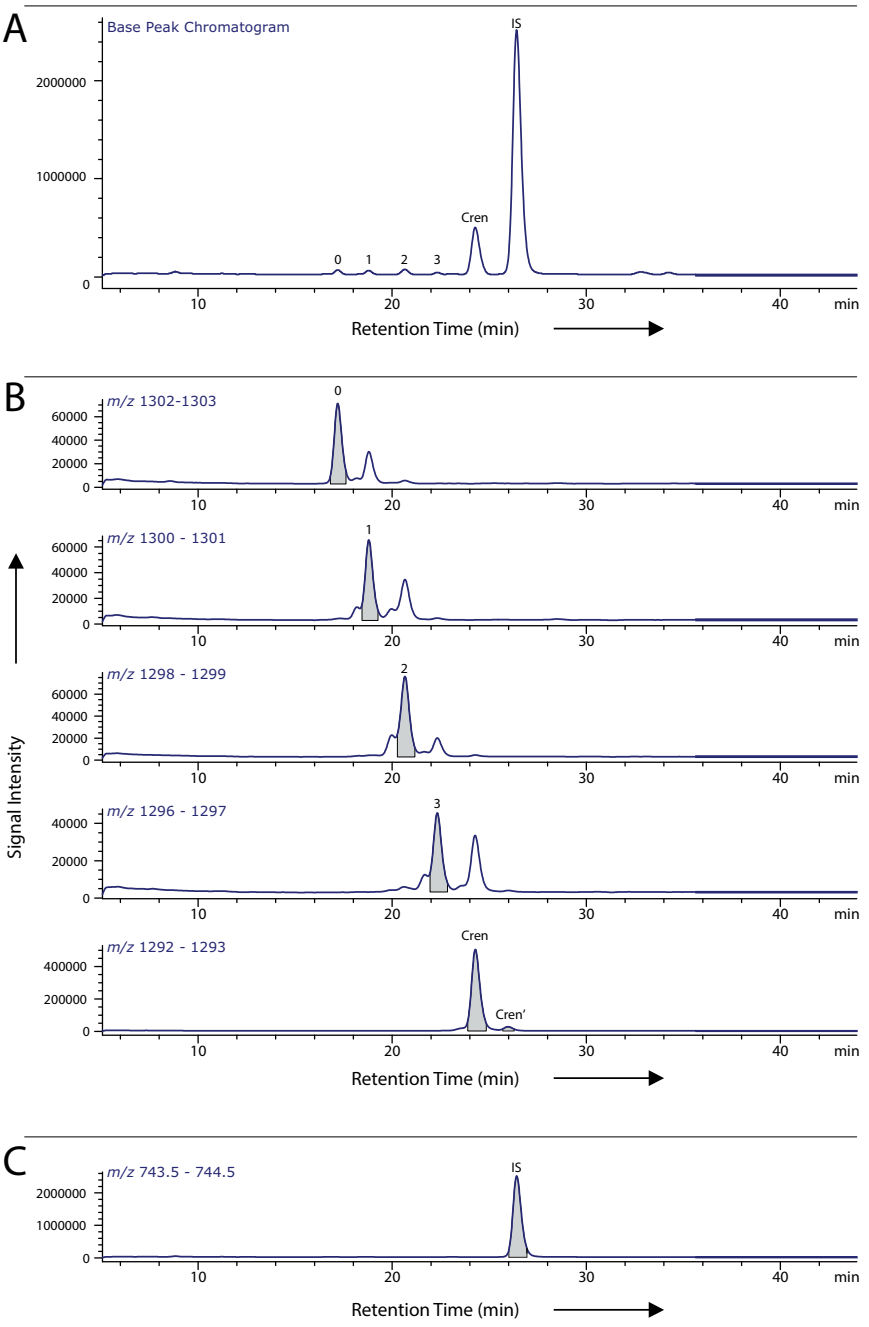

Fig. S8. Partial HPLC/MS base peak chromatogram and mass chromatograms of a typical sample (95Br-59). Numbers refer to the GDGT numbers in Eq. **S3**. (*A*) Partial HPLC/MS base peak chromatogram. (*B*) Mass chromatograms of the GDGTs used in the determination of TEX_{86}. Integrated peak areas are indicated in gray. (*C*) Mass chromatogram of the internal standard (IS) added for quantification purposes.

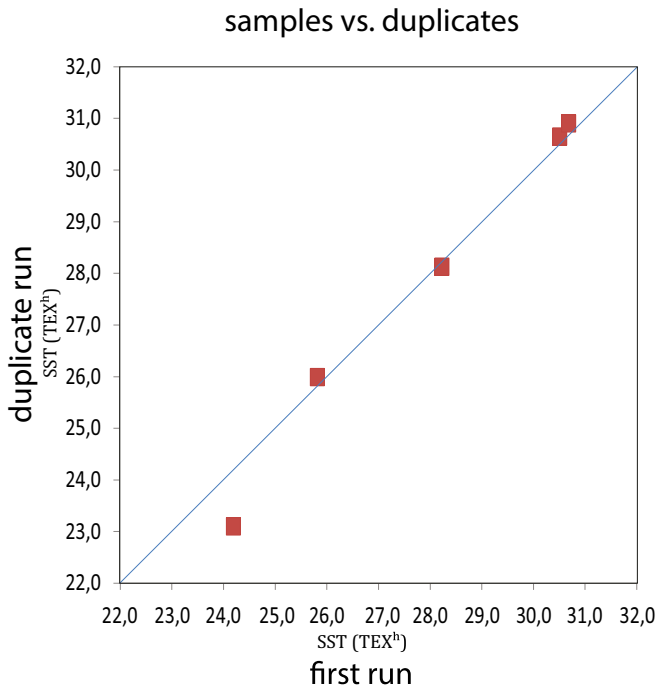

Fig. S9. TEX_{86}-derived sea surface temperatures of samples processed in duplicate relative to their original values.

Table S1. A list of samples used in our study, with the distance from the base of Unit F indicated

			Analyzed for			
Sample code	Distance from base Unit F	Lithological unit	Grain size	Planktic foraminifera	Dinocysts	TEX_{86} and BIT-index
95BR 60	420.00	Littig Member	X	X		X
95BR 59	395.00	Littig Member	X	X	X	X
95BR 58	370.00	Littig Member	X	X	X	
95BR 57	345.00	Littig Member	X	X	X	X
95BR 56	320.00	Littig Member	X	X	X	
95BR 55	295.00	Littig Member	X	X	X	X
95BR 54	285.00	Unit I	X	X	X	
95BR 53	275.00	Unit I	X	X	X	X
95BR 52	265.00	Unit I	X	X	X	
95BR 51	255.00	Unit I	X	X	X	
95BR 50	245.00	Unit I	X	X	X	
95BR 49	240.00	Unit I	X	X	X	X
95BR 48	235.00	Unit I	X	X	X	
95BR 47	230.00	Unit I	X	X	X	X
smBR 27	225.00	Unit I			X	X
95BR 46	225.00	Unit I	X	X	X	
95BR 45	220.00	Unit I	X	X	X	
95BR 44	215.00	Unit I	X	X	X	
95BR 43	210.00	Unit I	X	X	X	
95BR 42	205.00	Unit I	X	X	X	X
95BR 41	200.00	Unit I	X	X	X	X
95BR 40	195.00	Unit I	X	X	X	
95BR 39	190.00	Unit I	X	X	X	X
95BR 38	185.00	Unit I	X	X	X	
95BR 37	180.00	Unit I	X	X	X	X
95BR 36	175.00	Unit I	X	X	X	
95BR 35	170.00	Unit I	X	X	X	X
95BR 34	165.00	Unit I	X	X	X	X
95BR 33	160.00	Unit I	X	X	X	
95BR 32	155.00	Unit I	X	X	X	X
95BR 31	150.00	Unit I	X	X	X	X
95BR 30	145.00	Unit I	X	X	X	X
95BR 29	140.00	Unit I	X	X	X	X
95BR 28	135.00	Unit I	X	X	X	
95BR 27	130.00	Unit I	X	X	X	X
95BR 26	125.00	Unit I	X	X	X	
95BR 25	120.00	Unit I	X	X	X	X
95BR 24	115.00	Unit I	X	X	X	
95BR 23	110.00	Unit I	X	X	X	
95BR 22	105.00	Unit I	X	X	X	
95BR 21	100.00	Unit I	X	X	X	X
95BR 20	95.00	Unit I	X	X	X	X
95BR 19	90.00	Unit I	X	X	X	X
95BR 18	85.00	Unit I	X	X	X	
95BR 17	80.00	Unit I	X	X	X	X
sm BR 24	75.00	Unit I			X	X
95BR 16	75.00	Unit I	X	X	X	
95BR 15	70.00	Unit I	X	X	X	
95BR 14	65.00	Unit I	X	X	X	X
95BR 13	60.00	Unit I	X	X	X	
95BR 12	55.00	Unit I	X	X	X	X
95BR 11	50.00	Unit I	X	X	X	X
95BR 10	45.00	Unit I	X	X	X	X
95BR 9	40.00	Unit I	X	X	X	X
95BR 8	35.00	Unit I	X	X	X	X
sm BR82 233	33.00	Unit I			X	X
95BR 7	30.00	Unit I	X	X	X	
sm BR82 232	28.00	Unit H			X	X
95BR 6	27.00	Unit H	X	X	X	
95BR 5	23.00	Unit G	X	X	X	
95BR 5Bo	23.00	Unit G				X

Table S1. Cont.

Sample code	Distance from base Unit F	Lithological unit	Analyzed for			
			Grain size	Planktic foraminifera	Dinocysts	TEX_{86} and BIT-index
95BR 4B	22.00	Unit G	X	X	X	
95BR 5On	21.00	Unit G				X
95BR 4A	20.00	Unit G	X	X	X	
BR2-4–7.5	17.90	Unit G	X	X		X
BR2-4–7	17.40	Unit G	X	X		X
BR2-4–6.5	16.90	Unit G	X	X		
BR2 4–6	16.40	Unit G	X	X		X
BR2-4–5.5	15.90	Unit G	X	X		
BR2-4–5	15.40	Unit G	X	X		X
sm BR 20	15.00	Unit G			X	X
95BR 3	15.00	Unit G			X	
BR2-4–4.5	14.90	Unit G	X	X		
BR2-4–4	14.40	Unit G	X	X		X
BR2-4–3.5	13.90	Unit G	X	X		X
BR2-4–3	13.40	Unit G	X	X		
BR2-4–2.5	12.90	Unit G	X	X		
BR2-4–2	12.40	Unit G	X	X		
95BR 2	12.00	Unit G			X	
BR2-4–1.5	11.90	Unit G	X	X		X
BR2-4–1	11.40	Unit G	X	X		X
BR2-4–0.5	10.90	Unit G	X	X		X
95BR-1M	10.40	Unit F	X	X	X	X
95BR-1L	9.60	Unit F	X	X	X	X
95BR-1K	8.80	Unit F	X	X	X	
95BR-1J	8.00	Unit F	X	X	X	
95BR-1I	7.20	Unit F	X	X	X	X
95BR-1H	6.40	Unit F	X	X	X	X
95BR-1G	5.60	Unit F	X	X	X	X
95BR-1F	4.80	Unit F	X	X	X	X
95BR-1E	4.00	Unit F	X	X	X	X
95BR-1D	3.20	Unit F	X	X	X	X
95BR-1C	2.40	Unit F	X	X	X	
smBR82 8	2.00	Unit F			X	
95BR-1B	1.60	Unit F	X	X	X	X
95BR-1A	0.80	Unit F	X	X	X	
sm BR 11	−15.00	Event Bed Unit D			X	X
BR GSS	−20.00	Event Bed Unit C				X
smBR 8	−25.00	Event Bed Unit B			X	X
BR LM	−26.00	Shell hash				X
95BR 61	−30.00	Corsicana FM	X	X	X	
smBR 13	−32.00	Corsicana FM			X	X
smBR 12	−40.00	Corsicana FM			X	X
smBR 17	−52.50	Corsicana FM			X	X
95BR 62	−70.00	Corsicana FM	X	X	X	
95BR 63	−110.00	Corsicana FM	X	X	X	
smBR 3,04	−125.00	Corsicana FM			X	X
95BR 64	−150.00	Corsicana FM	X	X	X	
95BR 65	−190.00	Corsicana FM	X	X	X	
smBR 3,03	−225.00	Corsicana FM			X	X
95BR 66	−230.00	Corsicana FM	X	X	X	
95BR 67	−270.00	Corsicana FM	X	X	X	
95BR 68	−310.00	Corsicana FM	X	X	X	
smBR 3,02	−325.00	Corsicana FM			X	X
95BR 69	−350.00	Corsicana FM	X	X	X	
95BR 70	−390.00	Corsicana FM	X	X	X	
smBR 3,01	−425.00	Corsicana FM			X	X
95BR 72	−500.00	Corsicana FM	X	X	X	

For each sample, the table indicates from which lithological unit it comes and which analyses have been performed on it.